Excavated and dendritic Pt-Co nanocubes as efficient ethylene glycol and glycerol oxidation electrocatalysts

Hongyu Du[a,b], Kai Wang[a,b], Panagiotis Tsiakaras[c,d,e,*], Pei Kang Shen[a,b,*]

[a] Collaborative Innovation Center of Sustainable Energy Materials, Guangxi Key Laboratory of Electrochemical Energy Materials, State Key Laboratory of Processing for Non-ferrous Metal and Featured Materials, Guangxi University, Nanning, 530004, PR China
[b] School of Physics, School of Materials Science and Engineering, Sun Yat-sen University, Guangzhou, 510275, PR China
[c] Laboratory of Electrochemical Devices based on Solid Oxide Proton Electrolytes, Institute of High Temperature Electrochemistry, RAS, Yekaterinburg 620990, Russia
[d] Ural Federal University, 19 Mira Str., Yekaterinburg 620002, Russia
[e] Laboratory of Alternative Energy Conversion Systems, Department of Mechanical Engineering, School of Engineering, University of Thessaly, Pedion Areos, 38834, Greece

ARTICLE INFO

ABSTRACT

Noble metal electrocatalysts with excavated and dendritic architectures have recently attracted growing attention for their large accessible surface areas and high density of under-coordinated atoms. However, it is a tough challenge to avoid the atoms migrating to the corners and kinks and finally obtain the excavated structure, after the complicated interaction among multiple factors during the synthesis process, let alone the growth control of dendritic shape. Herein we demonstrate a facile strategy to synthesize Pt-Co nanocubes having excavated and dendritic structure (Pt-Co EDNCs). Specifically, the Pt-Co EDNC nanocrystal is composed of a deeply excavated nanocube and nanodendrites selectively protruding on the vertexes. Further electrocatalytic investigations showed that Pt-Co EDNCs exhibited enhanced catalytic properties towards the electro-oxidation of ethylene glycol and glycerol compared with commercial Pt/C, which could be attributed to both its unique structure and the synergism between Pt and Co.

1. Introduction

The global climate change and the continuous reduction of fossil fuel resources have forced people to search for new clean and renewable fuel (energy) sources and new highly efficient energy conversion devices [1,2]. Fuel cells, especially direct liquid fuel cells (DLFCs), are electrochemical devices that have recently attracted the interest of researchers for their high energy conversion efficiency, portability, and operation flexibility with a wide variety of fuels [3–5]. Even though direct methanol fuel cells (DMFCs) are the most investigated DLFCs, some polyhydric alcohols, such as ethylene glycol and glycerol, are much less volatile and less toxic compared to methanol [6,7]. Furthermore, the ethylene glycol and glycerol have higher theoretical energy density, and the long chain of these polyhydric alcohols can avoid crossover through the electrolyte membranes [8,9]. For these reasons, developing the direct ethylene glycol and glycerol (fed) fuel cells with higher performance is of great interest for many research groups world widely [10–13]. Concerning that the anode catalysts play a key role in the electrochemical process in the DLFCs, an efficient approach to meet this requirement is synthesizing catalysts with excellent catalytic activities for the anode oxidation reactions [14].

Pt-based nanocrystals are proved to be the state-of-the-art electrocatalysts for many electrochemical reactions, including the ethylene glycol and glycerol oxidation reactions (EGOR, GOR) [8,15]. However, the high cost and poor durability of Pt restrict its commercial application, so improving both utilization and properties has been the critical issue for the design of Pt-based catalysts [16]. Alloying Pt with other metals (M, M = Fe, Co, Ni, Cu, Pd, etc.) is regarded as an efficient strategy, and many highly-performing Pt-M alloys have been widely reported for their bifunctional mechanism and electronic effect [17–20]. In addition, it is well-known that the activity of electrocatalysts is highly dependent on the nanostructure [21–23]. Some nanocrystals with specific structures, such as nanodendrites or excavated structure [24–33], could expose more accessible surface area and more under-coordinated atoms (e.g., edges, corners, kinks), which can promote the enhancement of catalytic activity [34–36]. However, owing to the interaction among atomic diffusion, dissociation and redeposition in synthesis process [37,38], the high exposure of high energy facets and active sites are not thermodynamically favored [27]. Therefore, it is a big challenge to explore new synthesis mechanisms and efficient

* Corresponding authors.
  E-mail addresses: tsiak@mie.uth.gr (P. Tsiakaras), pkshen@gxu.edu.cn (P.K. Shen).

strategies for the fabrication of bimetallic nanocrystals with tailored and optimized structure.

Herein, we report a facile one-pot synthesis method of Pt-Co alloy nanocubes with unique excavated and dendritic structure. The nanocrystal can be regarded as the combination of excavated nanocube in the central region and dendrites on its vertexes. Moreover, the excavated nanocube can be regarded as the assembly of nanosheets bounded with {110} facets, which could expose more accessible high-energy surface area; while the dendrites on the vertexes can provide more under-coordinated atoms as active sites. Benefiting from the unique structure and bimetallic synergistic effect, the as-prepared nanocrystals showed enhanced properties in both ethylene glycol and glycerol electro-oxidation reactions.

2. Experimental

2.1. Chemical and materials

Chloroplatinic acid hexahydrate ($H_2PtCl_6·6H_2O$), oleylamine (OAm, 80–90%), cetyltrimethyl ammonium chloride (CTAC, 99%), didecyldimethyl ammonium chloride (DDAC, 99%) and cetyltrimethyl ammonium bromide (CTAB, 98%) were purchased from Aladdin Industrial Corporation, potassium hydroxide (KOH) was purchased from Guangzhou Chemical Reagent Factory, cobalt sulfate heptahydrate ($CoSO_4·7H_2O$), N, N-Dimethylformamide (DMF), hexane, ethanol, ethylene glycol and glycerol were purchased from Tianjin Damao Chemical Reagent Factory. The water was ultrapure deionized (DI) water (18.2 MΩ) in these experiments. All the reagents were used as received without further purification.

2.2. Synthesis of excavated and dendritic Pt-Co nanocubes (Pt-Co EDNCs)

In order to synthesize the Pt-Co EDNCs, H_2PtCl_6 (0.14 mL, 100 mg/mL), $CoSO_4·7H_2O$ (2.4 mg), CTAC (300 mg) were introduced into a Teflon vessel with oleylamine (10 mL) in sequence. The precursor solution was mixed uniformly under ultrasonication and kept stirring for 5 min, respectively, then sealed the vessel in a stainless steel. The vessel was then heated at 170 °C for 6 h with vigorous magnetic stirring. After cooling down to the room temperature, the final products were collected by centrifugation and washed with ethanol for three times.

2.3. Characterization

Transmission electron microscopy (TEM), high resolution-TEM (HRTEM) and high angle annular dark field scanning transmission electron microscope (HAADF-STEM) images were performed on a FEI Tecnai G2 F30 transmission electron microscope at an accelerating voltage of 300 kV. The line-scanning was performed on the EDX detector equipped on the FEI Talos F200, elemental energy-dispersive X-ray (EDX) spectroscopy mapping was performed on the EDX detector equipped on the FEI Tecnai G2 F30. SEM images were taken with Hitachi SU8220 apparatus. The X-ray diffraction (XRD) measurements were collected on a D/Max-IIIA, using Cu-Kα radiation (Rigaku Co., Japan). The inductively coupled plasma atomic emission spectroscopy (TJA RADIAL IRIS 1000 ICP-AES, USA) was employed to determine the compositions of the samples for the electrochemical reactions. The X-ray photoemission (photoelectron) spectroscopy (XPS) spectra were obtained with a Thermo Fisher Scientific ESCALAB 250 photoelectron spectrometer equipped with a monochromatic Al Kα X-ray source. The final oxidation products of ethylene glycol and glycerol oxidation reactions were detected by high-performance liquid chromatography (HPLC, HP1100 Hewlett Packard, USA).

2.4. Electrochemical measurements

The electrochemical measurements were performed in a three-compartment electrochemical cell, glassy carbon electrode in a diameter of 5 mm covered with the catalysts worked as working electrode and graphite bar was used as counter electrode, saturated calomel electrode (SCE) and KCl saturated Ag/AgCl was used as reference electrode, respectively. The cyclic voltammetry (CV) curves were recorded by a biopotentiostat (AFCBP1E, Pine Instrument Co., USA). The carbon supported catalysts were prepared and used after depositing on the glassy carbon. In a typical preparation procedure, commercial carbon (Vulcan-72) was dispersed with the Pt-Co EDNCs and nanoclusters (NCs) in the n-butylamine, respectively. The as prepared solution was ultrasonicated for 1 h and kept on stirring for 72 h. Then, the catalysts were collected by using ethanol and washed three times with methanol to remove the n-butylamine. The working electrode was prepared by adding uniform catalyst ink (prepared above) onto the surface of the glassy carbon electrode; when the ink became an exsiccated catalyst layer, the working electrode was immersed into electrolyte. The Pt loadings of the catalysts were controlled in the order of 10 μg_{Pt} cm^{-2} on the electrode, and then determined by ICP-AES. The activation of the electrode was performed by sweeping from -0.2 V to 1.0 V vs. SCE at a scan rate of 100 mV s^{-1} in N_2-saturated 0.5 M H_2SO_4 solution for 100 cycles, then the CV curves were recorded at 50 mV s^{-1} in the N_2-saturated 0.5 M H_2SO_4 solution. The ethylene glycol oxidation reaction (EGOR) and glycerol oxidation reaction (GOR) were performed by sweeping from -0.8 V to 0.4 V vs. Ag/AgCl at a scan rate of 50 mV s^{-1} in 0.5 M ethylene glycol + 0.5 M KOH and 0.1 M glycerol + 1 M KOH, respectively. The stability was tested by chronoamperometry experiments carried out at a constant potential of 0.2 V vs. Ag/AgCl for 10,000 s and 5000 s for EGOR and GOR, respectively. The electrolytes used in the electrochemical measurements were all kept at 30 °C.

3. Results and discussion

3.1. Structure characterization of samples

A facile one-pot solvothermal method was applied to synthesize excavated dendritic Pt-Co nanocubes (Pt-Co EDNC). In a typical synthesis, H_2PtCl_6, $CoSO_4$, and cetyltrimethylammonium chloride (CTAC) were dispersed uniformly in oleylamine (OAm), and sealed in a Teflon-lined stainless steel autoclave after ultrasonic treatment. Then, the autoclave was heated at 170 °C under rapid stirring and maintained for 6 h before it was cooled down to room temperature (details in the Experimental Section). The final products were washed by ethanol for three times. The as-prepared products were then characterized in detail. As can be seen from the high angle annular dark field scanning transmission electron microscopy (HAADF-STEM) images and from transmission electron microscopy (TEM) in Fig. 1a, b and S1, the nanocrystals have uniform square outline, and the average edge length of the nanocrystals is about 46.92 nm (Figure S2). Then, we have characterized an individual nanocrystal from different orientations. In Fig. 1e, the nanocrystal looks like a letter "X" based on [001] orientation, and interestingly the dendrites only grow on the vertexes. Moreover, in Fig. 1c, a perfect six-arm nanocrystal is obtained along [111] orientation. These typical projections indicate that the nanocrystal presents a unique excavated and dendritic structure; the central part of the nanocrystal is excavated nanocube, and the vertexes are occupied by nanodendrites. To further confirm our hypothesis, a 3D model was proposed, and a series of TEM images of an individual nanocrystal were obtained by tilting it to different angles (Figure S3, S4).

As seen in Fig. 1d, e and S3, the 3D model fits pretty well with each corresponding TEM image. The high-resolution TEM (HRTEM) image (Fig. 1f) and the corresponding fast Fourier transform (FFT) pattern (Figure S3b) of an individual nanocrystal indicates that the nanocrystals are highly-crystallized. The lattice fringe spaces are measured to be 0.195 nm and 0.137 nm, which can be indexed to {200} and {220} planes, respectively. These two values are just between the lattice spacing of standard Pt and Co face-centered cubic (fcc) structure,
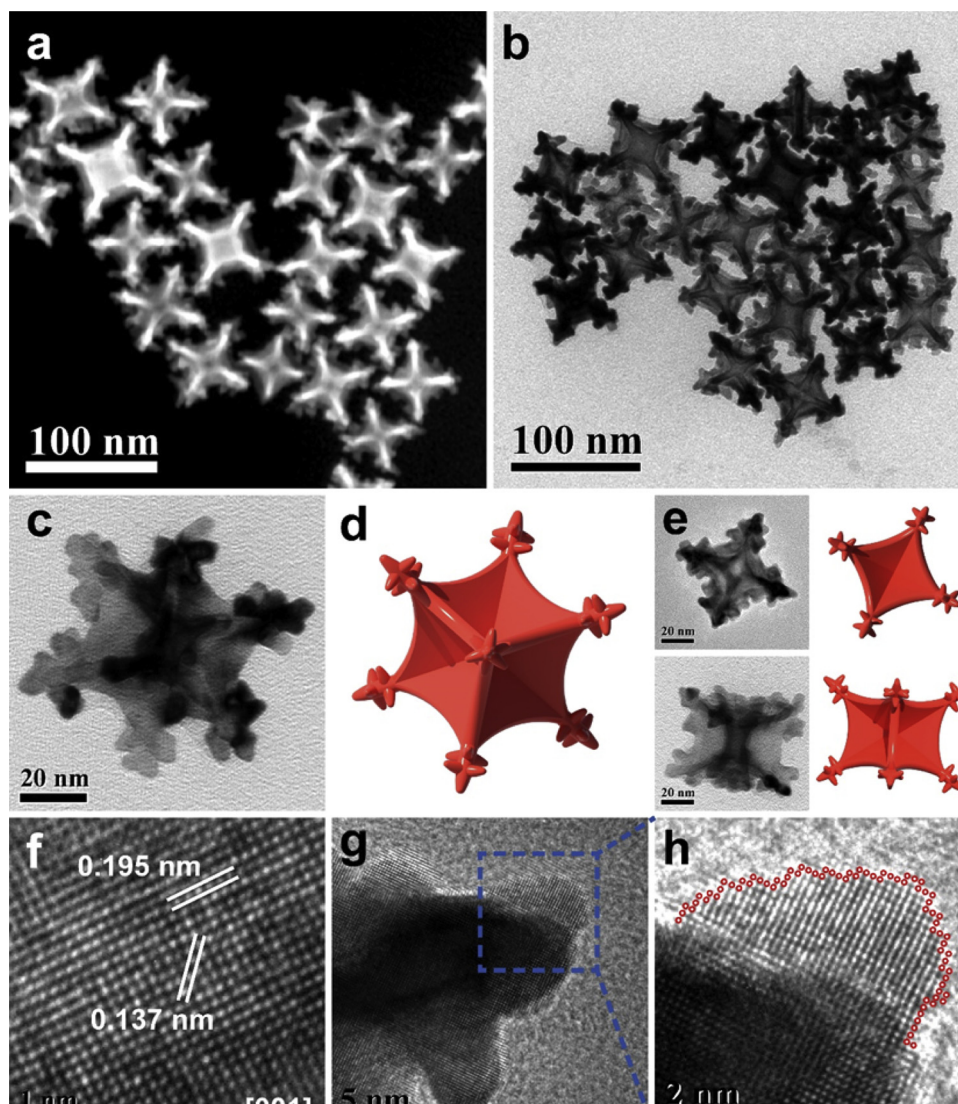
Fig. 1. The typical (a) HAADF-STEM and (b) TEM images of Pt-Co EDNCs. (c, d, e) TEM images of individual Pt-Co EDNCs obtained from [111], [001] and [011] orientation and corresponding 3D models. (f) HRTEM image in [001] orientation. (g) TEM image of the nanodendrites on the vertex and the (h) HRTEM taken from the dotted square in (g).

demonstrating the successful alloying of Pt and Co [39]. Fig. 1g shows the HRTEM of the dendrites taken from the vertex of the nanocrystal, which further confirms the dendritic structure, and clearly shows the overgrowth of branches at multiple sites on the vertex of the nanocrystal. In addition, abundant high-index facets and low-coordinated atoms can be observed around the surface (Fig. 1h).

The composition and element distribution of the Pt-Co EDNCs were further revealed by energy-dispersive X-ray (EDX) spectroscopy elemental mapping. According to Fig. 2a, the spatial distribution of Pt and Co are uniform in the whole excavated dendritic nanocube. The line-scanning profile also indicates this result (Fig. 2b).

The EDX measurement shows that the Pt/Co atomic ratio is 82.6:17.4 (Fig. 2c), which was further confirmed by inductively coupled plasma atomic emission spectroscopy (ICP-AES) (Table S1). The XRD pattern of the Pt-Co EDNCs is slightly shifted to the higher degree (right) compared with Pt PDF standard card, which is consistent with the high atomic ratio of Pt/Co, but it still indicates the formation of the Pt–Co alloy (Fig. 2d). Furthermore, the XPS spectrum shows that the Pt 4f binding energy of the Pt-Co EDNCs is blue-shifted in comparison to that of pure Pt, which means the shifted d-band center of Pt-Co EDNCs (Figure S5) [40].

In order to shed light to the growth mechanism of Pt-Co EDNCs, the intermediate nanocrystals at different synthesis stages were characterized to investigate the shape-evolution process. As shown in Fig. 3a, some polyhedral nanocrystals appear after 0.5 h. After 2 h of reaction time, small excavated nanocubes were formed with an average edge length of 21.4 nm (Fig. 3b).

At the reaction time of 4 h, the average edge length of the excavated nanocubes was increased to 41.27 nm, and some small dendrites were observed (Fig. 3c). When it comes to 6 h, the nanocrystals and dendrites grow larger, and the final Pt-Co EDNCs were synthesized (Fig. 3d). The morphology evolution process shows that the excavated nanocrystals firstly appeared after the first 2 h, and its size increased as time went on; during this process, nanodendrites selectively grow onto the vertexes of nanocubes. Then the nanodendrites grew bigger, and finally the excavated dendritic structure was synthesized. A corresponding scheme was then made to show these processes (Fig. 3e).

To further understand the formation mechanism of the as-prepared nanocrystal, we then explore the role of multiple synthesis factors, which may directly influence the formation of the nanocrystals. CTAC was often used as the capping agent in controlling the structure of metal nanocrystals, so we firstly investigated the role of CTAC in the present synthesis system [41–43]. Fig. 4 shows that, in the absence of CTAC, nanoclusters of Pt-Co alloy were formed (the size of clusters is about
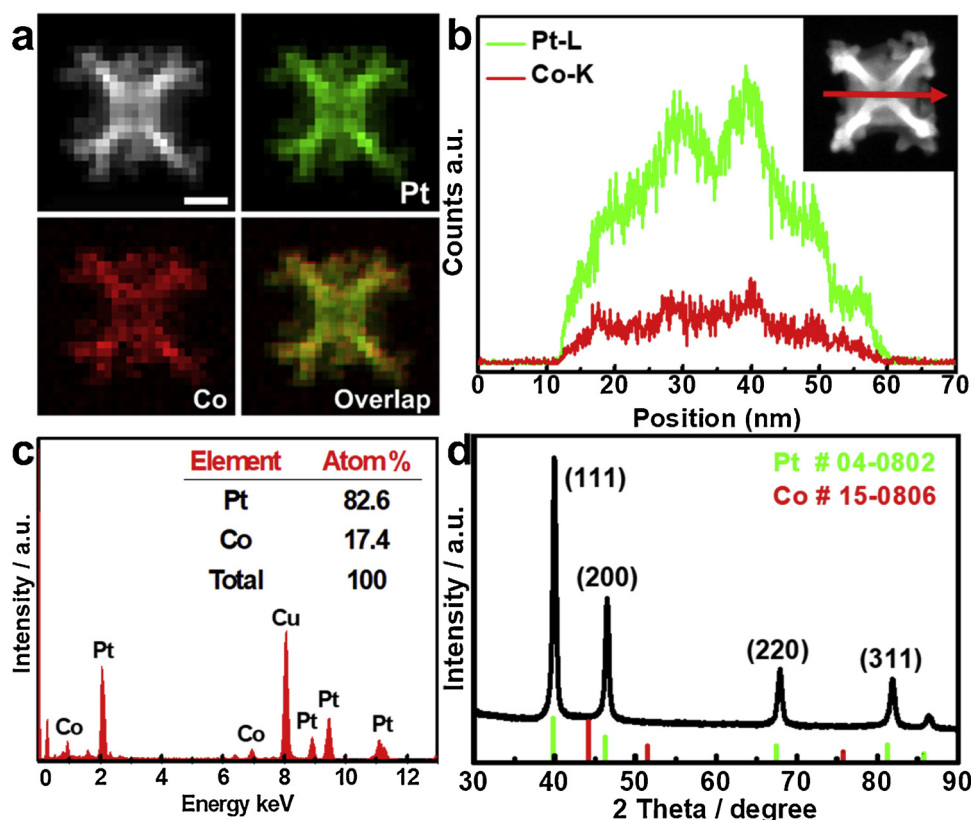
Fig. 2. (a) HAADF-STEM image and elemental mapping images of an individual Pt-Co EDNC, the scale bar is 20 nm. (b) line-scanning profiles (recorded across the red line in the inset), (c) EDX spectrum and (d) XRD pattern of Pt-Co EDNCs (For interpretation of the references to colour in this figure legend, the reader is referred to the web version of this article.).
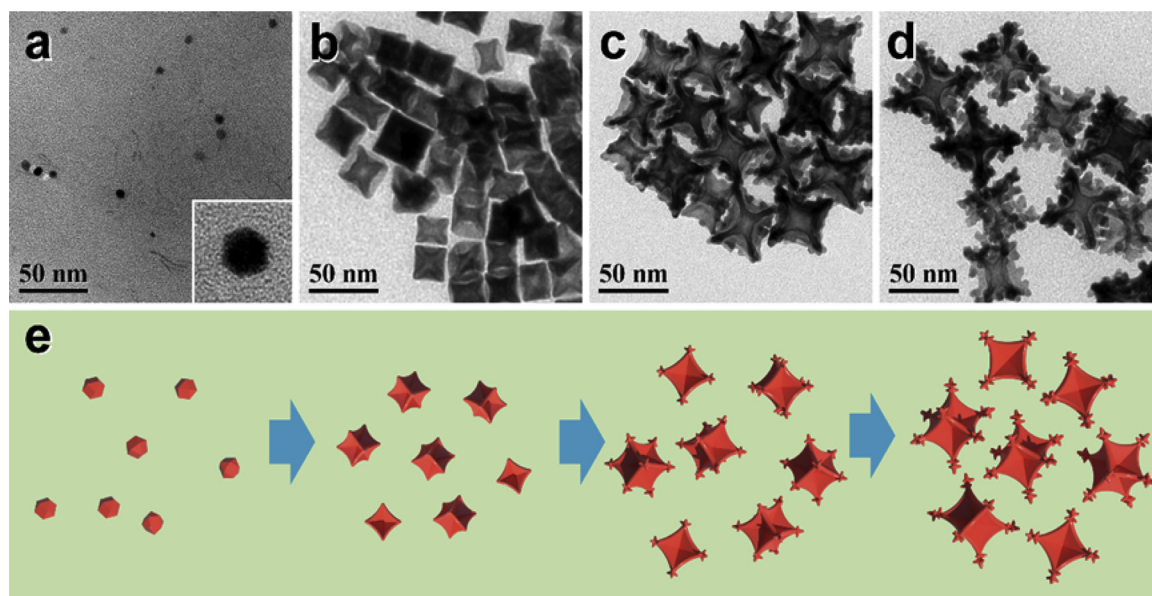

Fig. 3. TEM images of the intermediate nanocrystals obtained at different reaction times: (a) 30 min, (b) 2 h, (c) 4 h and (d) 6 h. (e) Corresponding 3D models for the shape evolution process of Pt-Co EDNCs.

59.05 nm). When we introduced 100 mg CTAC into the precursors, the final products showed a trend to be like cubic nanoclusters (the edge length of cubic clusters is about 51.81 nm).

When the amount of CTAC was increased to be 200 mg, the dendritic and excavated nanocubic outline started to appear. Finally, when we introduced 300 mg CTAC into the precursor, well-defined excavated dendritic Pt-Co nanocubes were synthesized.

From Fig. 4d, it can distinguish that the nanodendrites are mainly distributed on the vertexes of the nanocubes compared with Fig. 4 These results indicate that the presence of CTAC could promote the

formation of the excavated cubic structure of Pt-Co nanocrystals in this reaction system, and more abundant CTAC would limit the overgrowth of dendrites on the concave surfaces of nanocubes. In addition, we also investigated the influence of CTAC by replacing it with DDAC and CTAB (Figure S6). To sum up, an appropriate amount of CTAC is the key issue for the formation of excavated dendritic nanocubes.

We then investigated the products synthesized at different temperature values (Figure S7). When the temperature was decreased from 170 °C to 140 °C, no products were synthesized, which means that the reducing ability of this reaction system is not enough to synthesize Pt-
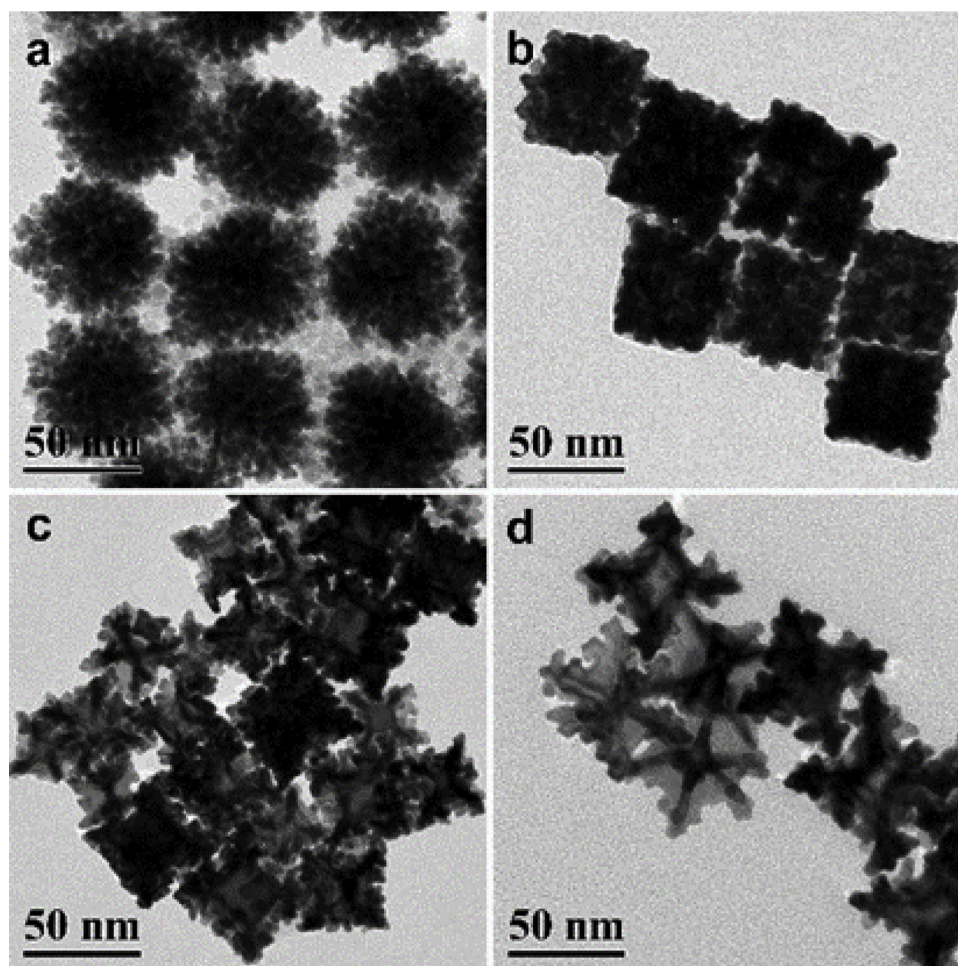
Fig. 4. TEM images of Pt-Co nanocrystals synthesized with different feeding amounts of CTAC in the precursor solution: (a) 0 mg, (b) 100 mg, (c) 200 mg and (d) 300 mg.

Co alloy nanocrystals at this temperature. When the temperature is 150 °C, the final products are excavated Pt-Co nanocubes and no nanodendrites were observed on their vertices. When the temperature was increased to 190 °C, nanocubic clusters with overgrown nanodendrites were obtained. These results indicate that the temperature directly influences the growth of the dendrites on the nanocubes.

According to the experimental explorations above, a possible formation mechanism of Pt-Co EDNCs was proposed. In this reaction system, the CTAC and temperature are two main factors in the formation process, and the controlling of formation can be regarded as the competition between the capping agent and reducing ability of system (Figs. 4, S7 & S8). On the one hand, CTAC acts as capping agent and leads to the formation of excavated nanocubes of Pt-Co alloy, which was confirmed by the experimental results and previous literature findings [29]. On the other hand, the results show that the reducing ability of the reaction system was positively related to temperature [44]. When temperature is lower, the capping agent played a dominant role in the reaction process, both concave surfaces and vertexes were capped, and the nanocrystals tended to be excavated nanocubes. When the temperature was too high, the influence of capping agent relatively reduced and all attachable sites of nanocrystals were activated, the final products tended to be cubic clusters. When the system was set in a proper temperature, owing to the energy differences between the concave surface and vertexes, only the active sites on the vertexes were activated and the adatoms deposited on these sites, and finally the Pt-Co nanocubes with excavated and dendritic structure were successfully synthesized [45,46].

3.2. Electrochemical performance of the samples

The Pt-Co EDNCs and Pt-Co nanoclusters (Pt-Co NCs, Fig. 4a) loaded on carbon were used as electrocatalysts for both EGOR and GOR (Figure S9). The commercial Pt/C were also tested in the same conditions for comparison (see the Experimental Section for details). The electrochemically active surface areas (ECSA) were firstly determined by hydrogen adsorption in the cyclic voltammograms (CV) recorded in N_2-saturated 0.5 M H_2SO_4 solution (scan rate: 50 mV s^{-1}. Normalized to geometrical surface area of working electrode. Fig. 5a).

The ECSA of Pt-Co EDNC/C (32.62 mA/cm^2) was larger than Pt-Co NC/C (24.38 mA/cm^2), which was consistent with the highly exposed morphology characterized above (Figure S10).

Fig. 5b and c show the EGOR and GOR CV curves (normalized to ECSAs) recorded at a scan rate of 50 mV s^{-1} in 0.5 M ethylene glycol + 0.5 M KOH and 0.1 M glycerol + 1 M KOH, respectively. As shown in Fig. 5d, the specific activities of Pt-Co EDNC/C, Pt-Co NC/C and commercial Pt/C are 7.82 (2.12-fold higher than that of commercial Pt/C), 6.00, 3.68 mA/cm^2 for EGOR, and 3.53 (2.30-fold higher than that of commercial Pt/C), 2.78, 1.53 mA/cm^2 for GOR, respectively. In addition, Pt-Co EDNC/C also possesses the highest mass activities for both EGOR and GOR, respectively (Figure S11). The highest rank of Pt-Co EDNC/C indicates the enhanced performance for the EGOR and GOR, which may be ascribed to the positive role of the large accessible high energy facets and under-coordinated atoms around the surface, and the synergetic effect between Pt and Co.

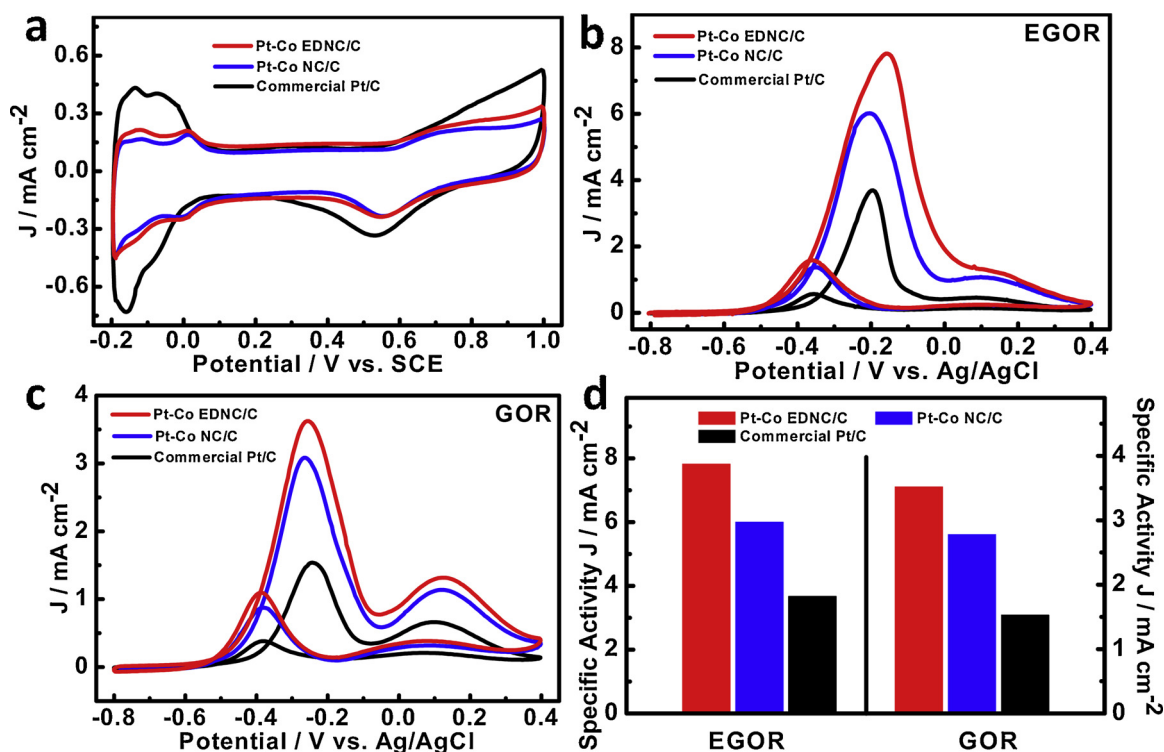The electrochemical stability of the as synthesized electrocatalysts

Fig. 5. Cyclic voltammetry (CV) curves of different catalysts recorded (a) in N$_2$-saturated 0.5 M H$_2$SO$_4$ solution (scan rate of 50 mV s^{-1}, normalized to geometrical surface area of working electrode), (b) 0.5 M ethylene glycol + 0.5 M KOH and (c) 0.1 M glycerol + 1 M KOH, respectively (scan rate: 50 mV s^{-1}, normalized to the electrochemically active surface areas). (d) Specific activities of different catalysts for EGOR and GOR.

was then evaluated by the aid of chronoamperometric (CA) measurements. The catalysts were tested at -0.2 V vs. Ag/AgCl in the corresponding electrolytes. As can be seen in Figure S12, the current density of Pt-Co EDNC/C exhibits a much slower decay than Pt-Co NC/C and commercial Pt/C in both EGOR and GOR. Over the entire tests in ethylene glycol (10,000 s) and glycerol (5000 s), the current densities of Pt-Co EDNC/C still remained the highest rank among these three catalysts, which indicated the enhanced electrochemical stabilities for both of EGOR and GOR. The TEM and EDX results of Pt-Co EDNC/C were performed after the long-term durability test. The TEM image shows that there was no obvious morphology change of the Pt-Co EDNCs, and the EDX results show that the element ratio of Pt and Co comes to be 5.29:1 (match well with the result of ICP-AES) (Figure S13, Table S2). The slight reducing of Co content could be caused by the electrochemical dealloying of Co during the electrochemical measurement [47]. The oxidation products in the electrolyte were also investigated by HPLC after durability test. Oxalic acid, glycolic acid and formic acid were detected after EGOR. Oxalic acid, tartronic acid, glycolic acid & glyceric acid and formic acid were detected after GOR (Figs S14, S15, S16, and S17) [6,48,49].

4. Conclusions

In summary, we presented a facile one-pot method to synthesize Pt-Co nanocubes with excavated and dendritic structure, by the precise control of reaction system reducing ability and amount of CTAC. A series of experiments were carried out to investigate the formation process of the nanocrystals, and it was proposed that the overgrowth of dendrites on the vertexes of the excavated nanocubes might be ascribed to the control of capping agents and the system temperature. In addition, the as-prepared nanocrystals exhibit an enhanced performance for both EGOR and GOR, which could be attributed to the synergetic effects between Pt and Co, high exposure of high energy facets and undercoordinated atoms. We expect that this work could be extended to the

design and synthesis of other novel Pt-based catalysts with excavated and dendritic structure for various practical applications.

Declarations of interest

None.

Appendix A. Supplementary data

Supplementary material related to this article can be found, in the online version, at doi:https://doi.org/10.1016/j.apcatb.2019.117951.

References

[1] M.S. Dresselhaus, I.L. Thomas, Alternative energy technologies, Nature 414 (2001) 332–337.
[2] S. Chu, A. Majumdar, Opportunities and challenges for a sustainable energy future, Nature 488 (2012) 294.
[3] G.L. Soloveichik, Liquid fuel cells, Beilstein J. Nanotechnol. 5 (2014) 1399–1418.
[4] U.B. Demirci, Direct liquid-feed fuel cells: thermodynamic and environmental concerns, J. Power Sources 169 (2007) 239–246.
[5] B.C. Ong, S.K. Kamarudin, S. Basri, Direct liquid fuel cells: a review, Int. J. Hydrogen Energy 42 (2017) 10142–10157.
[6] K. Matsuoka, Y. Iriyama, T. Abe, M. Matsuoka, Z. Ogumi, Electro-oxidation of methanol and ethylene glycol on platinum in alkaline solution: poisoning effects and product analysis, Electrochim. Acta 51 (2005) 1085–1090.
[7] H. Liu, C. Song, L. Zhang, J. Zhang, H. Wang, D.P. Wilkinson, A review of anode

catalysis in the direct methanol fuel cell, J. Power Sources 155 (2006) 95–110.

[8] N. Zhang, Y. Feng, X. Zhu, S. Guo, J. Guo, X. Huang, Superior bifunctional liquid fuel oxidation and oxygen reduction electrocatalysis enabled by PtNiPd core–shell nanowires, Adv. Mater. 29 (2017) 1603774.

[9] E. Peled, V. Livshits, T. Duvdevani, High-power direct ethylene glycol fuel cell (DEGFC) based on nanoporous proton-conducting membrane (NP-PCM), J. Power Sources 106 (2002) 245–248.

[10] A. Serov, C. Kwak, Recent achievements in direct ethylene glycol fuel cells (DEGFC), Appl. Catal. B: Environ. 97 (2010) 1–12.

[11] R.B. de Lima, V. Paganin, T. Iwasita, W. Vielstich, On the electrocatalysis of ethylene glycol oxidation, Electrochim. Acta 49 (2003) 85–91.

[12] Z. Zhang, L. Xin, J. Qi, D.J. Chadderdon, W. Li, Supported Pt, Pd and Au nanoparticle anode catalysts for anion-exchange membrane fuel cells with glycerol and crude glycerol fuels, Appl. Catal. B: Environ. 136-137 (2013) 29–39.

[13] A. Zalineeva, A. Serov, M. Padilla, U. Martinez, K. Artyushkova, S. Baranton, C. Coutanceau, P.B. Atanassov, Self-supported PdxBi catalysts for the electrooxidation of glycerol in alkaline media, J. Am. Chem. Soc. 136 (2014) 3937–3945.

[14] N. Tian, Z.-Y. Zhou, S.-G. Sun, Y. Ding, Z.L. Wang, Synthesis of tetrahexahedral platinum nanocrystals with high-index facets and high electro-oxidation activity, Science 316 (2007) 732.

[15] Y. Feng, L. Bu, S. Guo, J. Guo, X. Huang, 3D platinum–lead nanowire networks as highly efficient ethylene glycol oxidation electrocatalysts, Small 12 (2016) 4464–4470.

[16] I. Bar-On, R. Kirchain, R. Roth, Technical cost analysis for PEM fuel cells, J. Power Sources 109 (2002) 71–75.

[17] V.R. Stamenkovic, B.S. Mun, M. Arenz, K.J.J. Mayrhofer, C.A. Lucas, G. Wang, P.N. Ross, N.M. Markovic, Trends in electrocatalysis on extended and nanoscale Pt-bimetallic alloy surfaces, Nat. Mater. 6 (2007) 241–247.

[18] S. Luo, M. Tang, P.K. Shen, S. Ye, Atomic-scale preparation of octopod nanoframes with high-index facets as highly active and stable catalysts, Adv. Mater. 29 (2017) n/a-n/a.

[19] Y. Yu, W. Yang, X. Sun, W. Zhu, X.Z. Li, D.J. Sellmyer, S. Sun, Monodisperse MPt (M = Fe, Co, Ni, Cu, Zn) nanoparticles prepared from a facile oleylamine reduction of metal salts, Nano Lett. 14 (2014) 2778–2782.

[20] D.F. van der Vliet, C. Wang, D. Li, A.P. Paulikas, J. Greeley, R.B. Rankin, D. Strmcnik, D. Tripkovic, N.M. Markovic, V.R. Stamenkovic, Unique electrochemical adsorption properties of Pt-Skin surfaces, Angew. Chemie 124 (2012) 3193–3196.

[21] Y. Xia, Y. Xiong, B. Lim, S.E. Skrabalak, Shape-controlled synthesis of metal nanocrystals: simple chemistry meets complex physics? Angew. Chemie Int. Ed. 48 (2009) 60–103.

[22] M.H. Huang, P.-H. Lin, Shape-controlled synthesis of polyhedral nanocrystals and their facet-dependent properties, Adv. Funct. Mater. 22 (2012) 14–24.

[23] K. Wang, H. Du, R. Sriphathoorat, P.K. Shen, Vertex-type engineering of Pt–Cu–Rh heterogeneous nanocages for highly efficient ethanol electrooxidation, Adv. Mater. 30 (2018) 1804074.

[24] B. Lim, M. Jiang, P.H.C. Camargo, E.C. Cho, J. Tao, X. Lu, Y. Zhu, Y. Xia, Pd-Pt bimetallic nanodendrites with high activity for oxygen reduction, Science 324 (2009) 1302.

[25] R.G. Weiner, S.E. Skrabalak, Metal dendrimers: synthesis of hierarchically stellated nanocrystals by sequential seed-directed overgrowth, Angew. Chemie Int. Ed. 54 (2015) 1181–1184.

[26] L.-M. Lacroix, C. Gatel, R. Arenal, C. Garcia, S. Lachaize, T. Blon, B. Warot-Fonrose, E. Snoeck, B. Chaudret, G. Viau, Tuning complex shapes in platinum nanoparticles: from cubic dendrites to fivefold stars, Angew. Chemie Int. Ed. 51 (2012) 4690–4694.

[27] Q. Chen, Z. Cao, G. Du, Q. Kuang, J. Huang, Z. Xie, L. Zheng, Excavated octahedral Pt-Co alloy nanocrystals built with ultrathin nanosheets as superior multifunctional electrocatalysts for energy conversion applications, Nano Energy 39 (2017)

582–589.

[28] Q. Chen, Y. Yang, Z. Cao, Q. Kuang, G. Du, Y. Jiang, Z. Xie, L. Zheng, Excavated cubic platinum–tin alloy nanocrystals constructed from ultrathin nanosheets with enhanced electrocatalytic activity, Angew. Chemie 128 (2016) 9167–9171.

[29] H. Du, S. Luo, K. Wang, M. Tang, R. Sriphathoorat, Y. Jin, P.K. Shen, High-quality and deeply excavated Pt3Co nanocubes as efficient catalysts for liquid fuel electrooxidation, Chem. Mater. 29 (2017) 9613–9617.

[30] Y. Jia, Y. Jiang, J. Zhang, L. Zhang, Q. Chen, Z. Xie, L. Zheng, Unique excavated rhombic dodecahedral PtCu3 alloy nanocrystals constructed with ultrathin nanosheets of high-energy {110} facets, J. Am. Chem. Soc. 136 (2014) 3748–3751.

[31] Q. Chen, Y. Jia, S. Xie, Z. Xie, Well-faceted noble-metal nanocrystals with non-convex polyhedral shapes, Chem. Soc. Rev. 45 (2016) 3207–3220.

[32] J. Zhang, H. Li, J. Ye, Z. Cao, J. Chen, Q. Kuang, J. Zheng, Z. Xie, Sierpinski gasket-like Pt–Ag octahedral alloy nanocrystals with enhanced electrocatalytic activity and stability, Nano Energy 61 (2019) 397–403.

[33] B.Y. Xia, H.B. Wu, X. Wang, X.W. Lou, Highly concave platinum nanoframes with high-index facets and enhanced electrocatalytic properties, Angew. Chemie Int. Ed. 52 (2013) 12337–12340.

[34] Z.L. Wang, T.S. Ahmad, M.A. El-Sayed, Steps, ledges and kinks on the surfaces of platinum nanoparticles of different shapes, Surf. Sci. 380 (1997) 302–310.

[35] F. Tao, Excavation of precious-metal-based alloy nanoparticles for efficient catalysis, Angew. Chemie Int. Ed. 55 (2016) 15212–15214.

[36] Z.-Y. Jiang, Q. Kuang, Z.-X. Xie, L.-S. Zheng, Syntheses and properties of micro/nanostructured crystallites with high-energy surfaces, Adv. Funct. Mater. 20 (2010) 3634–3645.

[37] D.W. Bassett, P.R. Webber, Diffusion of single adatoms of platinum, iridium and gold on platinum surfaces, Surf. Sci. 70 (1978) 520–531.

[38] M. Villarba, H. Jónsson, Diffusion mechanisms relevant to metal crystal growth: Pt/Pt(111), Surf. Sci. 317 (1994) 15–36.

[39] B.Y. Xia, H.B. Wu, N. Li, Y. Yan, X.W. Lou, X. Wang, One-pot synthesis of Pt–Co alloy nanowire assemblies with tunable composition and enhanced electrocatalytic properties, Angew. Chemie 127 (2015) 3868–3872.

[40] V.R. Stamenkovic, B.S. Mun, K.J.J. Mayrhofer, P.N. Ross, N.M. Markovic, Effect of surface composition on electronic structure, stability, and electrocatalytic properties of Pt-transition metal alloys: Pt-skin versus Pt-skeleton surfaces, J. Am. Chem. Soc. 128 (2006) 8813–8819.

[41] J. Zhang, M.R. Langille, M.L. Personick, K. Zhang, S. Li, C.A. Mirkin, Concave cubic gold nanocrystals with high-index facets, J. Am. Chem. Soc. 132 (2010) 14012–14014.

[42] M. Chen, B. Wu, J. Yang, N. Zheng, Small adsorbate-assisted shape control of Pd and Pt nanocrystals, Adv. Mater. 24 (2012) 862–879.

[43] K. Jiang, D. Zhao, S. Guo, X. Zhang, X. Zhu, J. Guo, G. Lu, X. Huang, Efficient oxygen reduction catalysis by subnanometer Pt alloy nanowires, Sci. Adv. 3 (2017).

[44] A. Chen, P. Holt-Hindle, Platinum-based nanostructured materials: synthesis, properties, and applications, Chem. Rev. 110 (2010) 3767–3804.

[45] J. Huang, Y. Zhu, M. Lin, Q. Wang, L. Zhao, Y. Yang, K.X. Yao, Y. Han, Site-specific growth of Au–Pd alloy horns on Au nanorods: a platform for highly sensitive monitoring of catalytic reactions by surface enhancement Raman spectroscopy, J. Am. Chem. Soc. 135 (2013) 8552–8561.

[46] P. Liu, R. Qin, G. Fu, N. Zheng, Surface coordination chemistry of metal nanomaterials, J. Am. Chem. Soc. 139 (2017) 2122–2131.

[47] L. Huang, X. Zhang, Y. Han, Q. Wang, Y. Fang, S. Dong, High-index facets bounded platinum–lead concave nanocubes with enhanced electrocatalytic properties, Chem. Mater. 29 (2017) 4557–4562.

[48] Y. Kwon, M.T.M. Koper, Combining voltammetry with HPLC: application to electro-oxidation of glycerol, Anal. Chem. 82 (2010) 5420–5424.

[49] H. Wang, L. Thia, N. Li, X. Ge, Z. Liu, X. Wang, Selective electro-oxidation of glycerol over Au supported on extended poly(4-vinylpyridine) functionalized graphene, Appl. Catal. B: Environ. 166-167 (2015) 25–31.